Correlation-Enhanced Odd-Parity Interorbital Singlet Pairing in the Iron-Pnictide Superconductor LiFeAs

R. Nourafkan[1], G. Kotliar[2], and A.-M.S. Tremblay[1,3]

[1]*Département de Physique and Institut quantique, Université de Sherbrooke, Sherbrooke, Québec, Canada J1K 2R1*
[2]*Department of Physics & Astronomy, Rutgers University, Piscataway, NJ 08854-8019, USA and*
[3]*Quantum Materials Program, Canadian Institute for Advanced Research, Toronto, Ontario, M5G 1Z8, Canada*

The rich variety of iron-based superconductors and their complex electronic structure lead to a wide range of possibilities for gap symmetry and pairing components. Here we solve in the two-Fe Brillouin zone the full frequency-dependent linearized Eliashberg equations to investigate spin-fluctuations mediated Cooper pairing for LiFeAs . The magnetic excitations are calculated with the random phase approximation on a correlated electronic structure obtained with density functional theory and dynamical mean field theory. The interaction between electrons through Hund's coupling promotes both the intra-orbital $d_{xz(yz)}$ and the inter-orbital magnetic susceptibility. As a consequence, the leading pairing channel, conventional s^{+-}, acquires sizeable inter-orbital $d_{xy} - d_{xz(yz)}$ singlet pairing with odd parity under glide-plane symmetry. The combination of intra- and inter-orbital components makes the results consistent with available experiments on the angular dependence of the gaps observed on the different Fermi surfaces.

LiFeAs is a stoichiometric superconductor with superconducting $T_c \simeq 18$ K and no magnetic ordering. [1] Despite rather poor nesting [2–5], recent quasiparticle interference experiments identify the antiferromagnetic (AF) spin-fluctuation mediated mechanism as the predominant pairing interaction. [6] ARPES and quasiparticle-scattering interference measurements below T_c show that the superconducting (SC) gaps of LiFeAs are nodeless, with a Fermi surface (FS) dependence and a sizable variation along each FS. [2, 7, 8] Polarized neutron diffraction as a function of temperature has shown a suppression of the local spin susceptibility in the SC phase, suggesting singlet pairing. [9, 10]

In theoretical studies, the AF spin-fluctuation mediated pairing [11–14] and a combination of AF spin-fluctuation and orbital fluctuation mediated by phonons have been investigated. [15, 16] However, all studies are performed in the one-iron unit cell with various unfolding algorithms used to embed the correct symmetry. [17–21] This procedure is exact only for computing in-plane pairing. In addition, the SC gap equation is usually projected on the FS, the pairing interaction is symmetrized, [11] and the resulting equation is always solved in the BCS approximation. All of the above simplifications must be questioned before we can be confident of the results. Furthermore, for Fe-based superconductors (FeSCs) with a non-symmorphic point-group, [22] anti-symmetry of fermions does not place a constraint on the parity of the SC pairing channel. [23, 24] This allows for even-parity $d_{xz} - d_{yz}$ inter-orbital pairing [25], or for $d_{xy} - d_{xz(yz)}$ odd parity spin singlet pairing when there is orbital weight at the Fermi level from orbitals with different in-plane mirror reflection symmetry [26].

Hence, here we revisit spin-fluctuation mediated pairing by considering both Fe-$3d$ and As-$4p$ orbitals in the two-Fe unit cell. We solve the linearized Eliashberg equations [27] in the two-Fe Brillouin Zone (BZ) to investigate SC pairing and gap symmetry. Since there is increasing evidence that superconductivity does not emerge as a FS instability [40], we work in the orbital representation instead of projecting the gap equation on the FSs. Our results show that in the leading channel, with the conventional s^{+-} symmetry, odd parity inter-orbital pairing accompanies the usual intra-orbital pairing and increases with interactions, in particular with Hund's coupling. In contrast to previous studies [8, 11–13] we find that this state can reproduce the angular dependence of the gap on the electron pockets.

Electronic structure In LiFeAs, the bandwidth observed in ARPES is narrower than in LDA calculations and there are experimental evidences of long-lived magnetic moments. [9] This indicates the importance of correlations, so we employ the LDA+DMFT method to obtain the electronic structure. [41–43] Fig. 1 illustrates the LDA+DMFT partial spectral weight, $A_{ll}(\mathbf{k}, 0)$, of Fe t_{2g}- orbitals d_{xy} and $d_{xz,yz}$ on the FSs of LiFeAs. [44] The Fe e_g orbitals d_{z^2} and $d_{x^2-y^2}$ hybridize with As-p orbitals and contribute to the spectral weight lying above and below the Fermi level. The FS consists of three hole-like and two electron-like sheets around the center and corners of the BZ respectively. The two inner hole pockets are predominantly composed from d_{xz} and d_{yz} orbitals. The smallest hole pocket crosses the Fermi level only in close vicinity to the Γ point. It hybridizes with the d_{z^2} orbital near Z point and is closed there, while remaining $2D$ away from this point. The middle pocket has moderate k_z dispersion. The large hole-like Fermi surface originates purely from in-plane d_{xy} orbitals and therefore is $2D$ without noticeable k_z dispersion. The electron pockets are made from an admixture of d_{xy}, d_{xz} and d_{yz} orbitals. The electron pockets intersect at small k_z and their order flips, i.e., the inner pocket at $k_z = 0$ is the outer pocket at $k_z = \pi/c$.

Comparison to LDA, [27] shows that in LDA+DMFT: (a) The two inner hole pockets shrink while the outer one expands. (b) The middle hole pocket also deforms and takes on a butterfly shape at small k_z. [45] (c) At finite k_z, the outer
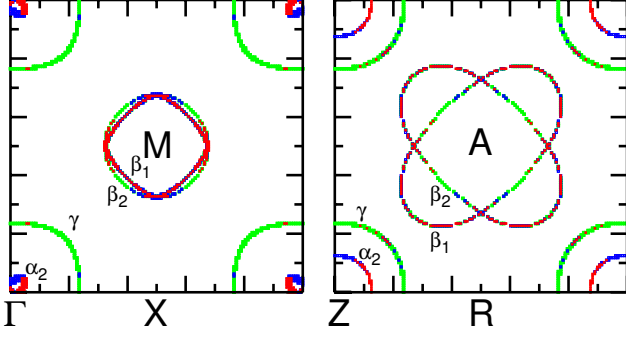
FIG. 1. (Color online) Partial spectral weight, $A_{ll}(\mathbf{k}, 0)$, of Fe t_{2g}- orbitals on the FS in the k_x-k_y plane with $k_z = 0$ (left), and $k_z = \pi/c$ (right) obtained from the LDA+DMFT calculation. Here the d_{xy}, d_{xz}, and d_{yz} orbitals are illustrated by green, blue and red colors, respectively. The α_1 pocket crosses the Fermi level only in close vicinity to the Γ point (not visible on this scale).
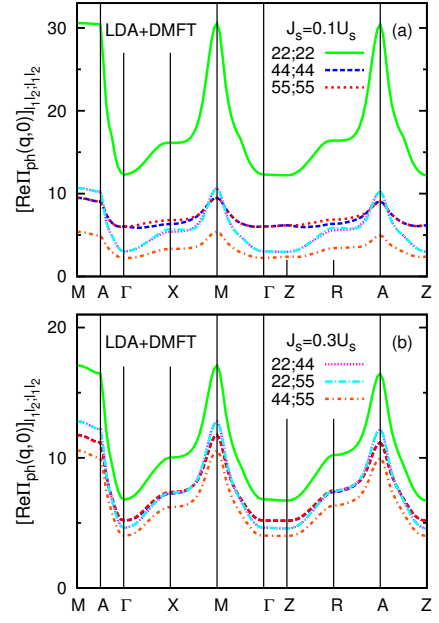

FIG. 2. (Color online) Several components of the pairing interaction of LiFeAs at $k_B T = 0.01$ eV in the particle-hole channel. There are two sets of screened interaction parameters yielding the same magnetic Stoner factor, namely $J_s = 0.1 U_s$, $U_s = 2.4$ eV on the top and $J_s = 0.3 U_s$, $U_s = 1.68$ eV on the bottom. The legend for the color coding is spread over both figures.

hole-pocket acquires some d_{xz} and d_{yz} orbital weight in the direction of the A point. (d) The shrinkage of the two inner hole pockets leads to larger patches where d_{xz} and d_{yz} orbitals mix on these pockets. (e) The electron pockets are moderately expanded and they become closer to each other. [27]

The t_{2g} orbitals are the most strongly correlated [43, 45] as is apparent from the mass enhancements $m^*/m_{LDA} = 2.0$, 1.85, 3.13 and 2.7 for d_{z^2}, $d_{x^2-y^2}$, d_{xy}, and $d_{xz,yz}$ orbitals, respectively. The d_{xy} orbital has the strongest mass enhancement and shortest quasi-particle lifetime.

Effective pairing interaction A SC instability in the singlet channel occurs when the corresponding pairing susceptibility diverges as one lowers temperature. A divergent susceptibility signals the appearance of a pole in the corresponding reducible complex vertex function, which describes all scattering processes of two propagating particles. Using the Bethe-Salpeter equation, the condition for an instability is that an eignvalue of the matrix $-\mathbf{\Gamma}^{irr,s}\chi^0_{pp}$ becomes unity. Here $\mathbf{\Gamma}^{irr,s}$ is the irreducible vertex function (effective pairing interaction) in the singlet channel, and χ^0_{pp} is the bare susceptibility in the particle-particle (p-p) channel. [27, 46, 47]

The density/magnetic fluctuations contribute to the pairing interaction by entering the ladder vertex defined by $\mathbf{\Pi}_{ph} \equiv -(1/2)\mathbf{\Gamma}^{irr,d}\chi^d_{ph}\mathbf{\Gamma}^{irr,d} + (3/2)\mathbf{\Gamma}^{irr,m}\chi^m_{ph}\mathbf{\Gamma}^{irr,m}$ where $\chi^{m(d)}_{ph}$ and $\mathbf{\Gamma}^{irr,m(d)}$ denote respectively the dressed susceptibility and the irreducible vertex function in the magnetic (density) channel. [27] These vertices can be calculated in the DMFT approximation. [48] However, such a calculation is prohibitively difficult for multiorbital systems at the low temperatures necessary to study superconductivity, [27] hence here we employ the random phase approximation (RPA). [49] In RPA, the irreducible vertex function is replaced by a static effective vertex which is parametrized by the *screened* intra-orbital Hubbard interaction, U_s, and the Hund's coupling J_s. [16, 27, 50, 51] The inter-orbital interaction and pair hopping are determined assuming spin-rotational symmetry. Note

that even though the static effective vertices U_s and J_s capture Kanamori-Brückner screening effects, they do not fully capture the dynamics of screening. In particular, the RPA treatment misses the fact that at high fermionic frequencies one should recover the bare interactions.

Fig. 2 shows the pairing interaction, $\mathbf{\Pi}_{ph}$, at $k_B T = 0.01$ eV for two sets of screened interaction parameters that yield the same magnetic Stoner factor. [52] Here we only present the intra-sublattice components because the inter-sublattice components are relatively small. In what follows, we focus on the Fe-1 and Fe-2 (on A and B sublattices respectively) t_{2g} orbitals: d_{xy} will be referred as 2 (7) and d_{xz} and d_{yz} as 4 (9) and 5 (10). The dominant effective pairing interaction components are repulsive. As can be seen in Fig. 2(a), due to better nesting, the d_{xy} intra-orbital $(22; 22)$ pairing vertex is dominant and the $d_{xz(yz)}$ intra-orbital $(44; 44)$ is sub-dominant, yet on average it is larger than inter-orbital vertices $(22; 44)$ and $(44; 55)$.

However, at larger J_s/U_s the situation changes. For a fixed Stoner factor (proximity to magnetic transition) upon increasing the J_s/U_s ratio from Fig. 2(a) to Fig. 2(b), the d_{xy} intra-orbital pairing component decreases while the $d_{xz(yz)}$ intra-orbital components and the inter-orbital components increase slightly. This shows that a higher J_s, through coupling to the more correlated d_{xy} orbital, compensates the decrease of spin susceptibility expected from the lower U_s (Fig. 2(b)). [27] Furthermore, since Hund's coupling correlates different orbitals, the inter-orbital components increase,
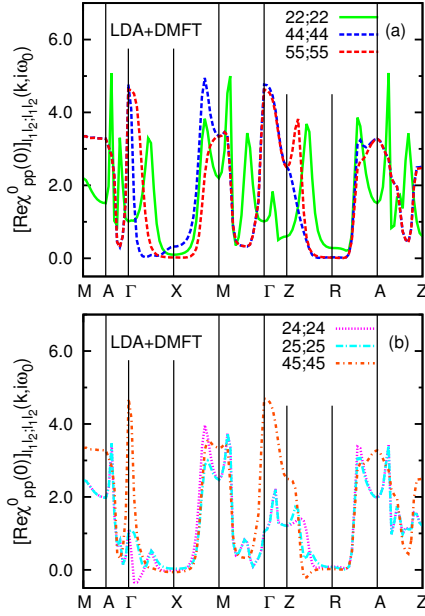
FIG. 3. (Color online) Real part of the several intra-sublattice components of the generalized particle-particle bare susceptibility at the lowest fermionic/bosonic Matsubara frequency.

becoming comparable with the $d_{xz(yz)}$ intra-orbital components. The d_{xy} intra-orbital vertex becomes less dominant at larger J_s/U_s. [53] This behavior of the magnetic susceptibility reflects itself directly in the pairing interaction (see supplemental material for the dressed susceptibilities in magnetic and charge channels).

Bare particle-particle susceptibility The generalized bare susceptibility in the p-p channel also enters the gap equation. [27] Fig. 3 shows the real part of several components of the generalized p-p bare susceptibility at the lowest fermionic/bosonic frequencies. The intra-orbital components are purely real. Both real and imaginary parts (see SM) show peaks at the position of FSs. For example, going from the Γ to the X point in the top panel, the three peaks are respectively related to the inner hole pocket with d_{xz} weight in close proximity to Γ, the middle pocket with d_{yz} weight and the outer pocket with d_{xy} weight. The peak heights are directly proportional to the corresponding orbital weight on the FSs and inversely proportional to the Fermi velocity. The peak widths are induced by correlation effects, implying that electrons near FSs may contribute to the Cooper pairing. In a non-interacting system the peak widths go to zero at zero temperature. [54] The larger $22;22$ peak component in the $M-\Gamma$ direction, compared with the $M-X(Y)$ direction, indicates that the SC gap on the outer electron pocket is larger in the $M-\Gamma$ direction.

In the BCS approximation, only real parts survive for the components considered here, due to a summation over Matsubara frequencies. In this case, the inter-orbital pairing is suppressed. Including the imaginary part in the full gap equation changes this trend. The imaginary parts of the inter-

orbital components change sign between corner and center of the BZ. They have some symmetries that transfer to the gap function: (i) They are odd under exchange of orbital indices, (ii) There is also a π phase difference between the two Fe ions (see SM).

SC pairing symmetry in LDA+DMFT+RPA The leading pairing channel is a channel with dominant d_{xy}, d_{xz} and d_{yz} intra-orbital pairing. In our gauge, the gap function components have both real and imaginary part which satisfy $\mathrm{Re}\Delta_{ll}^{AA(BB)} = -\mathrm{Im}\Delta_{ll}^{AA(BB)}$. All intra-orbital components change sign between center and corner of the BZ (see Fig. 4), as expected in conventional s^{+-} pairing. The d_{xy} intra-orbital component dominates, but has a small value on the γ pocket. The d_{xz} and d_{yz} intra-orbital components are out of phase, i.e. $\Delta_{55}^{AA(BB)} \simeq -\Delta_{44}^{AA(BB)}$ (not shown). They take large values on the $\alpha_{1,2}$ hole pockets. The inter-sublattice components are much smaller than intra-sublattice ones, $\mathbf{\Delta}^{AA(BB)} >> \mathbf{\Delta}^{AB(BA)}$. The largest inter-sublattice component is Δ_{22}^{AB}. In orbital basis, the gap functions do not change much between $k_z = 0$ and $k_z = \pi/c$, hence we present only $k_z = 0$ results.

In agreement with the above pairing-interaction analysis, upon increasing J_s/U_s the $d_{xz/yz}$ intra-orbital pairing strengthen. Furthermore, the d_{xy}-d_{xz} and d_{xy}-d_{yz} inter-orbital pairings increase. Although they vary on a smaller interval, they are comparable with the $d_{xz/yz}$ intra-orbital components on the electron FSs (compare Fig. 4 top and bottom panels).

We verify that the gap function components of the leading channel satisfy the relations $\Delta_{l_1 l_2}^{AA(BB)}(\mathbf{k}, i\omega_m) = \Delta_{l_1 l_2}^{BB(AA)}(-\mathbf{k}, i\omega_m)$, and $\Delta_{l_1 l_2}^{AA(BB)}(\mathbf{k}, i\omega_m) = \Delta_{l_2 l_1}^{AA(BB)}(-\mathbf{k}, -i\omega_m)$. [55] The first relation says that the superconducting state does not break parity: In LiFeAs the inversion center is located in the middle of Fe-Fe link. Under parity operation the sublattice A maps to sublattice B and vice versa and $\mathbf{k} \to -\mathbf{k}$. The components of the gap function also satisfy the relation $\Delta_{l_1 l_2}^{AA(BB)}(k_x, k_y, i\omega_m) = p_{l_1} p_{l_2} \Delta_{l_1 l_2}^{BB(AA)}(k_x, k_y, i\omega_m)$, where p_l denotes the parity of orbital l with respect to in-plane mirror reflection symmetry. [56] This symmetry is defined by in-plane mirror reflection followed by a half-translation, expressed in units of the two-Fe unit cell, $\{\sigma^z | \frac{1}{2}\frac{1}{2}0\}$. Thus, the intra-orbital components on the two Fe are equal, while the inter-orbital components between one even-parity (d_{xy}) and one odd-parity (d_{xz}, d_{yz}) orbital, change sign between two Fe-ions. These components are the parity-odd under $\{\sigma^z | \frac{1}{2}\frac{1}{2}0\}$ spin singlet pairings. [26] Furthermore, as can be seen from Fig. 4, the in-plane intra-orbital components satisfy $\Delta_{ll}^{AA(BB)}(k_x, k_y) = \Delta_{ll}^{AA(BB)}(-k_x, -k_y)$, while the inter-orbital components between d_{xy} and $d_{xz(yz)}$ satisfy $\Delta_{l_1 l_2}^{AA(BB)}(k_x, k_y) = -\Delta_{l_1 l_2}^{AA(BB)}(-k_x, k_y)$ or $\Delta_{l_1 l_2}^{AA(BB)}(k_x, k_y) = -\Delta_{l_1 l_2}^{AA(BB)}(k_x, -k_y)$.

Our calculations show that the gap symmetry of the leading channel is conventional s^{+-}. Indeed, although there is a
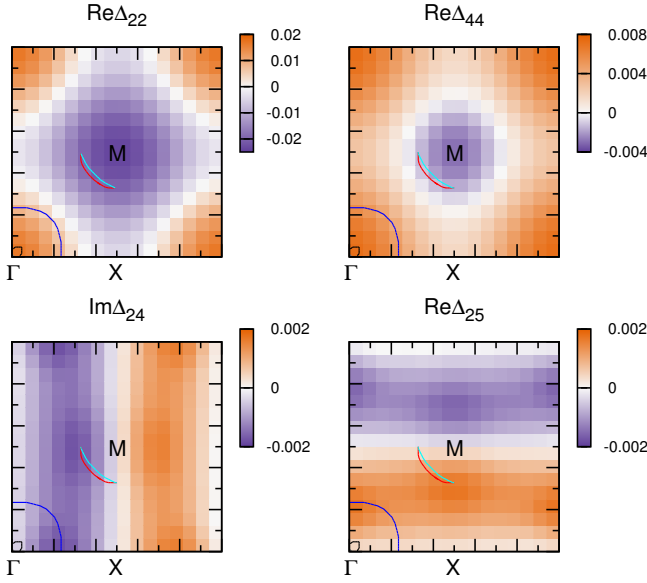
FIG. 4. (Color online) Top panels: The real part of the d_{xy} (left) and d_{xz} (right) in-plane intra-orbital components of the SC gap function at the lowest Matsubara frequency with largest eigenvalue in the orbital representation for $J_s/U_s = 0.3$ and $k_B T = 0.01$ eV. The imaginary part can be obtained from $\mathrm{Im}\Delta_{ll} = -\mathrm{Re}\Delta_{ll}$. Bottom panels: The real/imaginary part of the inter-orbital components of the SC gap function on sublattice A in the orbital representation, $\Delta_{l_1 l_2}^{AA}$. The corresponding components on sublattice B are out of phase with the displayed components, i.e. $\Delta_{l_1 l_2}^{BB} = -\Delta_{l_1 l_2}^{AA}$. The lines show one quarter of the Fermi surfaces.
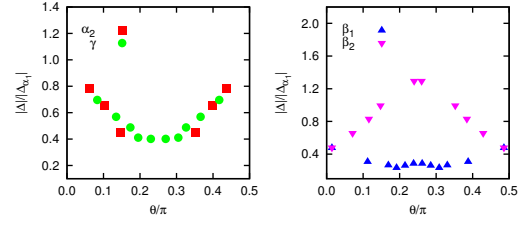

FIG. 5. (Color online) For $J_s/U_s = 0.3$, the SC gap magnitude (in units of the average gap magnitude on the α_1 pocket) as a function of the angle θ measured at the Γ and M points with respect to the x axis for $k_z = 0$ FSs.

phase difference between the d_{xz} and d_{yz} components of the gap function in the orbital basis, this phase difference is removed by another phase difference that arises when going to the Bloch basis corresponding to the $\alpha_{1,2}$ pockets. [27] In the *subleading* pairing channel, the d_{xy} intra-orbital component is in phase with d_{yz} and out of phase with d_{xz} intra-orbital components, which in the band representation gives s^{+-} gap symmetry with a sign change between $\alpha_{1,2}$ and γ pockets and between electron pockets and accidental nodes on the β_2 pocket. [14]

Finally, we comment on the SC gap magnitude on different FSs. [57] Diagonalizing the Bogoliubov quasi-particle Hamiltonian leads to a gap magnitude which has predominant $\cos 4\theta$ angular dependence on all pockets, as can be seen from Fig. 5. The angular dependence of the gap on the γ and of the average gap on the $\beta_{1,2}$ pockets are consistent with ARPES data: The gap is maximum at $\theta = 0, \pi/2$ and decreases when approaching $\theta = \pi/4$ (the direction toward M-point) on the γ pocket, while the average gap is maximum at $\theta = \pi/4$ (direction toward Γ-point) on the β pockets and decreases when approaching $\theta = 0, \pi/2$ where the two pockets cross. The gap on the β_2 electron pocket is increased in the direction of Γ-point due to a larger d_{xy} orbital content with a large pairing amplitude (see Fig. 4, upper panels). The gap on the β_1 electron pocket also shows a local enhancement at $\theta = \pi/4$.

Due to interchange of electron pockets as a function of k_z, the gap on the inner pocket becomes larger than that on the outer pocket at a finite k_z. Hence, for these pockets, a direct comparison with ARPES data has to take averaging over a range of k_z into account. [58] The ratio between the average gap magnitude on β pockets and γ pocket is also consistent with ARPES results [7, 8]. However, the gap magnitude on the α pockets is not the largest. This discrepancy with ARPES results may come from the fact that ARPES is performed at very low temperature while the linearized Eliashberg gap equation is valid at temperatures infinitesimally close to the transition temperature. The tunneling spectroscopy study of LiFeAs has shown a temperature evolution of superconductivity. [59] A calculation at a lower temperature shows that the sharp peaks in the 44 and 55 bare paring susceptibilities, Fig. 3(a), grow faster than the wider peak for 22. This leads to an increase of the gap on the α pockets at lower temperatures.

Conclusion Solving the full linearized Eliashberg gap equation with both real and imaginary parts and including correlations in the LDA+DMFT framework leads to a detailed description of the leading pairing channel in LiFeAs. Accounting for correlations in the spin fluctuation approach allows to correctly capture not only nesting effects but also Fe-d orbital fluctuating moments with orbitally dependent dynamics. Although the intra-orbital d_{xy} spin susceptibility is dominant, Hund's coupling between orbitals on individual Fe atoms promotes both the intra-orbital $d_{xz(yz)}$ component and the inter-orbital d_{xy}-$d_{xz(yz)}$ components of the magnetic susceptibility. As a consequence, the leading paring channel, conventional s^{+-}, acquires inter-orbital singlet pairing component with odd parity under glide-plane symmetry. This type of pairing may also be realized in other iron-based superconductors. Antiphase s^{+-} pairing [14] is sub-leading. The combination of inter-orbital odd-parity and intra-orbital even parity singlet pairing leads to a description of the angle-dependence and of the relative magnitudes of the gap on the β and γ Fermi surfaces that is consistent with state of the art experiments.

[1] J. H. Tapp, Z. Tang, B. Lv, K. Sasmal, B. Lorenz, P. C. W. Chu, and A. M. Guloy, Phys. Rev. B **78**, 060505 (2008).

[2] M. P. Allan, A. W. Rost, A. P. Mackenzie, Y. Xie, J. C. Davis, K. Kihou, C. H. Lee, A. Iyo, H. Eisaki, and T.-M. Chuang, Science **336**, 563 (2012).

[3] S. V. Borisenko, V. B. Zabolotnyy, D. V. Evtushinsky, T. K. Kim, I. V. Morozov, A. N. Yaresko, A. A. Kordyuk, G. Behr, A. Vasiliev, R. Follath, and B. Büchner, Phys. Rev. Lett. **105**, 067002 (2010).

[4] G. Lee, H. S. Ji, Y. Kim, C. Kim, K. Haule, G. Kotliar, B. Lee, S. Khim, K. H. Kim, K. S. Kim, K.-S. Kim, and J. H. Shim, Phys. Rev. Lett. **109**, 177001 (2012).

[5] P. M. R. Brydon, M. Daghofer, C. Timm, and J. van den Brink, Phys. Rev. B **83**, 060501 (2011).

[6] M. P. Allan, K. Lee, A. W. Rost, M. H. Fischer, F. Massee, K. Kihou, C.-H. Lee, A. Iyo, H. Eisaki, T.-M. Chuang, J. C. Davis, and E.-A. Kim, Nat. Phys. **11**, 177 (2015).

[7] K. Umezawa, Y. Li, H. Miao, K. Nakayama, Z.-H. Liu, P. Richard, T. Sato, J. B. He, D.-M. Wang, G. F. Chen, H. Ding, T. Takahashi, and S.-C. Wang, Phys. Rev. Lett. **108**, 037002 (2012).

[8] S. V. Borisenko, V. B. Zabolotnyy, A. A. Kordyuk, D. V. Evtushinsky, T. K. Kim, I. V. Morozov, R. Follath, and B. Bchner, Symmetry **4**, 251 (2012).

[9] J. D. Wright, M. J. Pitcher, W. Trevelyan-Thomas, T. Lancaster, P. J. Baker, F. L. Pratt, S. J. Clarke, and S. J. Blundell, Phys. Rev. B **88**, 060401 (2013).

[10] J. Brand, A. Stunault, S. Wurmehl, L. Harnagea, B. Büchner, M. Meven, and M. Braden, Phys. Rev. B **89**, 045141 (2014).

[11] Y. Wang, A. Kreisel, V. B. Zabolotnyy, S. V. Borisenko, B. Büchner, T. A. Maier, P. J. Hirschfeld, and D. J. Scalapino, Phys. Rev. B **88**, 174516 (2013).

[12] C. Platt, R. Thomale, and W. Hanke, Phys. Rev. B **84**, 235121 (2011).

[13] F. Ahn, I. Eremin, J. Knolle, V. B. Zabolotnyy, S. V. Borisenko, B. Büchner, and A. V. Chubukov, Phys. Rev. B **89**, 144513 (2014).

[14] Z. P. Yin, K. Haule, and G. Kotliar, Nat. Phys. **10**, 845 (2014).

[15] T. Saito, S. Onari, Y. Yamakawa, H. Kontani, S. V. Borisenko, and V. B. Zabolotnyy, Phys. Rev. B **90**, 035104 (2014).

[16] T. Yamada, J. Ishizuka, and Y. no, Journal of the Physical Society of Japan **83**, 043704 (2014).

[17] P. A. Lee and X.-G. Wen, Phys. Rev. B **78**, 144517 (2008).

[18] H. Eschrig and K. Koepernik, Phys. Rev. B **80**, 104503 (2009).

[19] O. Andersen and L. Boeri, Annalen der Physik **523**, 8 (2011).

[20] M. Casula and S. Sorella, Phys. Rev. B **88**, 155125 (2013).

[21] M. H. Fischer, New Journal of Physics **15**, 073006 (2013).

[22] V. Cvetkovic and O. Vafek, Phys. Rev. B **88**, 134510 (2013).

[23] J. Hu, Phys. Rev. X **3**, 031004 (2013).

[24] N. Hao and J. Hu, Phys. Rev. B **89**, 045144 (2014).

[25] T. Tzen Ong, P. Coleman, and J. Schmalian ArXiv e-prints (2014), arXiv:1410.3554.

[26] Y. Wang, T. Berlijn, P. J. Hirschfeld, D. J. Scalapino, and T. A. Maier, Phys. Rev. Lett. **114**, 107002 (2015).

[27] See supplemental material at [], which includes Refs. [28–39], for details of the electronic structure calculation, the spin fluctuation mediated pairing interaction and the RPA susceptibilities.

[28] S. Graser, T. A. Maier, P. J. Hirschfeld, and D. J. Scalapino, New Journal of Physics **11**, 025016 (2009).

[29] A. Toschi, A. A. Katanin, and K. Held, Phys. Rev. B **75**, 045118 (2007).

[30] G. Rohringer, A. Valli, and A. Toschi, Phys. Rev. B **86**, 125114 (2012).

[31] J. E. Hirsch and R. M. Fye, Phys. Rev. Lett. **56**, 2521 (1986).

[32] E. Gull, A. J. Millis, A. I. Lichtenstein, A. N. Rubtsov, M. Troyer, and P. Werner, Rev. Mod. Phys. **83**, 349 (2011).

[33] H. Hafermann, K. R. Patton, and P. Werner, Phys. Rev. B **85**, 205106 (2012).

[34] R. Yu, P. Goswami, Q. Si, P. Nikolic, and J. X. Zhu, Nat Commun **4**, 2783 (2013).

[35] J. Hu and H. Ding, Sci. Rep. **2**, 381 (2012).

[36] P. J. Hirschfeld, M. M. Korshunov, and I. I. Mazin, Reports on Progress in Physics **74**, 124508 (2011).

[37] T. Miyake, K. Nakamura, R. Arita, and M. Imada, Journal of the Physical Society of Japan **79**, 044705 (2010).

[38] T. Hajiri, T. Ito, R. Niwa, M. Matsunami, B. H. Min, Y. S. Kwon, and S. Kimura, Phys. Rev. B **85**, 094509 (2012).

[39] R. Nourafkan and A.-M. Tremblay, ArXiv e-prints (2016), arXiv:1601.05813.

[40] H. Miao, T. Qian, X. Shi, P. Richard, T. K. Kim, M. Hoesch, L. Y. Xing, X.-C. Wang, C.-Q. Jin, J.-P. Hu, and H. Ding, Nat Commun **6**, 7056 (2015).

[41] M. Aichhorn, L. Pourovskii, V. Vildosola, M. Ferrero, O. Parcollet, T. Miyake, A. Georges, and S. Biermann, Phys. Rev. B **80**, 085101 (2009).

[42] K. Haule, C.-H. Yee, and K. Kim, Phys. Rev. B **81**, 195107 (2010).

[43] Z. P. Yin, K. Haule, and G. Kotliar, Nat. Mater. **10**, 932 (2011).

[44] To keep a minimum variation of orbital content within a pocket, the electron pockets are chosen as inner and outer pockets β_1 and β_2 rather than as two crossed ellipse-like pockets of equal size.

[45] J. Ferber, K. Foyevtsova, R. Valentí, and H. O. Jeschke, Phys. Rev. B **85**, 094505 (2012).

[46] N. E. Bickers, "Self-consistent many-body theory for condensed matter systems," (Springer-Verlag, New York, 2004) Chap. 6, pp. 237–296.

[47] G. Esirgen and N. E. Bickers, Phys. Rev. B **57**, 5376 (1998).

[48] A. Toschi, R. Arita, P. Hansmann, G. Sangiovanni, and K. Held, Phys. Rev. B **86**, 064411 (2012).

[49] T. A. Maier, M. Jarrell, and D. J. Scalapino, Phys. Rev. B **75**, 134519 (2007).

[50] Y. Yanagi, Y. Yamakawa, and Y. Ōno, Phys. Rev. B **81**, 054518 (2010).

[51] H. Miyahara, R. Arita, and H. Ikeda, Phys. Rev. B **87**, 045113 (2013).

[52] The distance from magnetic and charge/orbital fluctuation criticality is determined by the corresponding (dimensionless) magnetic (density) Stoner factor $\alpha_{\mathbf{q}}^{m(d)}$, which is the largest eigenvalue of $\mathbf{\Gamma}^{irr,m}\chi_{ph}^0(\mathbf{q}, i\nu_n = 0)$ $(-\mathbf{\Gamma}^{irr,d}\chi_{ph}^0(\mathbf{q}, i\nu_n = 0))$.

[53] The $22; 44$ $(44; 55)$ components in the magnetic and charge susceptibilities in the p-h channel are related to the $24; 42$ and $42; 42$ $(45; 54$ and $54; 54)$ components of the pairing interac-

tion in the p-p channel.

[54] R. Nourafkan, Phys. Rev. B **93**, 241116 (2016).

[55] The combination of these relations gives $\Delta^{AA(BB)}_{l_1 l_2}(\mathbf{k}, i\omega_m) = \Delta^{BB(AA)}_{l_2 l_1}(\mathbf{k}, -i\omega_m)$.

[56] The five Fe $3d$ orbitals can be categorized into even orbital parity (d_{3z^2}, $d_{x^2-y^2}$, d_{xy}) with $p_l = +1$ and odd orbital parity (d_{xz}, d_{yz}) with $p_l = -1$.

[57] The linearized Eliashberg gap equation only gives gap symmetry, not gap magnitude. But to make contact with experiment one can approximately extract the relative size of the gaps on the different FSs. This can be done by defining a Bogoliubov quasi-particle Hamiltonian including the real part of the self-energy at the Fermi level in the normal part, and employing the gap function obtained from the gap equation as an estimate of the anomalous self-energy. [14] After diagonalizing the Bogoliubov quasi-particle Hamiltonian, the gap magnitude at momentum $\mathbf{k}$ is given by half of the difference between the smallest positive eigenvalue and the largest negative eigenvalue. This is the quasi-particle gap which reduces to the SC gap on the FSs. For this calculation, the gap function on a very dense $\mathbf{k}$-mesh is required. Since the gap function is a smooth function, its magnitude on a denser mesh can be obtained by spline interpolation.

[58] S. Borisenko, D. Evtushinsky, I. Morozov, S. Wurmehl, B. Bchner, A. Yaresko, T. Kim, M. Hoesch, T. Wolf, and N. Zhigadlo, "Direct observation of spin-orbit coupling in iron-based superconductors," (2014), arXiv:1409.8669.

[59] P. T. Nag, R. Schlegel, D. Baumann, H.-J Grafe, R. Beck, S. Wurmehl, B. Buchner, and C. Hess ArXiv e-prints (2015), arXiv:1509.03431.

Supplemental Materials: Correlation-Enhanced Odd-Parity Interorbital Singlet Pairing in the Iron-Pnictide Superconductor LiFeAs

Here, we present some details on the electronic structure of the LiFeAs in the first section. The Eliashberg equation and details of the calculation for the pairing interaction in the random phase approximation (RPA) and in the dynamical mean field theory (DMFT) are presented in the second section. We show how this calculation differs from the BCS approximation to these equations. Our results on the bare and dressed susceptibilities are presented in fourth section. Finally, we discuss some symmetries of the Green's function and their consequences on the susceptibilities.

ELECTRONIC STRUCTURE

LiFeAs crystallizes in a tetragonal structure with a space group $P4/nmm$. Fig. S1 shows the crystal structure of LiFeAs. In our study the crystal structure is fixed to the experimental structure.

We preformed a fully self-consistent LDA+DMFT calculation. [S1] We use a local Coulomb integral $U = F_0 = 4.0$ eV and a Hund's coupling $J = (F_2 + F_4)/14 = 0.8$ eV, where F_k are Slater integrals. [S2] We take the fully localized limit double-counting correction. We use $32 \times 32 \times 16$ $\mathbf{k}$-points and a rotationally invariant interaction matrix.

The momentum-resolved spectral function, $\text{Tr}\mathbf{A}(\mathbf{k}, \omega)$, (trace over all orbitals) along high-symmetry directions is displayed in Fig. S2, and compared with the LDA band structure. Compared to other pnictide families, LiFeAs has much shallower hole pockets around Γ. The flat top of these pockets implies a large density of states, [S3] which has been proposed to promote ferromagnetic fluctuations and triplet p-wave pairing. [S4] However, experiment supports singlet-pairing.

As can be seen from $\text{Tr}\mathbf{A}(\mathbf{k}, \omega)$, correlation effects lead to bandwidth reduction for the Fe-$3d$ states near the Fermi level: both the hole-pocket near the Γ point and the electron-pocket near the M-point are pushed towards the Fermi energy. The outer hole pocket becomes more incoherent.

The two low-energy hole-like bands at the Γ point form a degenerate doublet with the two-dimensional irreducible representation E_g. [S5] The subscript g and u denote the spatial even and odd parity respectively. The two degenerate eigenstates are predominantly given by $(ic_1(d^A_{xz} + d^B_{xz}) - c_2(d^A_{yz} + d^B_{yz}), ic_2(d^A_{xz} + d^B_{xz}) + c_1(d^A_{yz} + d^B_{yz}))$ where A, B refer to Fe ions and c_1, c_2 are real coefficients. Away from the Γ point, the symmetry reduces and the doublet splits. Depending on the $\mathbf{k}$-point, the eigenstate is composed predominantly from d_{xz}, or d_{yz} orbital, but a phase factor i between expansion coefficients is present everywhere. Along the high-symmetry lines Γ-M and Γ-X, the E_g symmetry reduces to one A_2 and one B_2 state.

The outer hole-like band at the Γ-point instead has B_{1g} symmetry with the $d^A_{xy} + d^B_{xy}$ Fe states. Along the high-
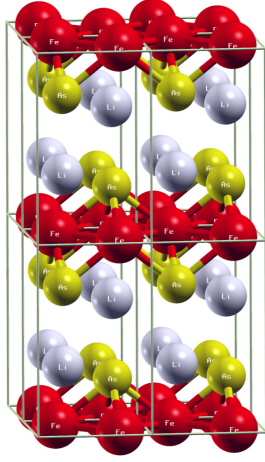
FIG. S1. (Color online) Crystal structure of LiFeAs. The structure is tetragonal with space group $P4/nmm$. Iron atoms are represented by red spheres, arsenic by yellow spheres. Light grey balls are larger cations, Li, between the layers. The c-axis points up. Note that a $2 \times 2 \times 2$ super-cell is plotted here. The FeAs layers are the electronically active part of the compound.

FIG. S3. (Color online) Fe t_{2g} character of the FSs at k_x-k_y plan with $k_z = 0$ (top panels), and $k_z = \pi/c$ (bottom panels) obtained from LDA calculation. Left, middle and right columns show d_{xy}, d_{xz} and d_{yz} orbitals respectively.
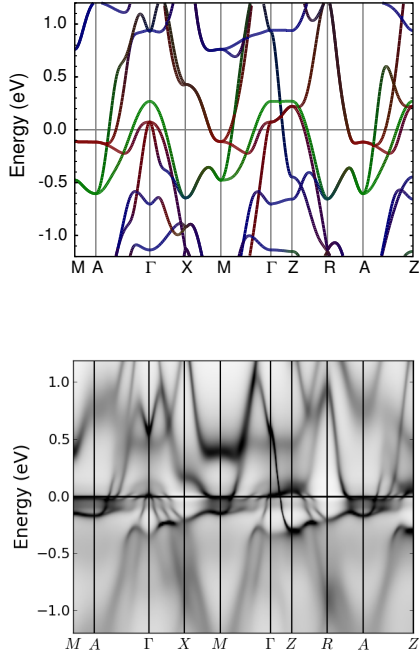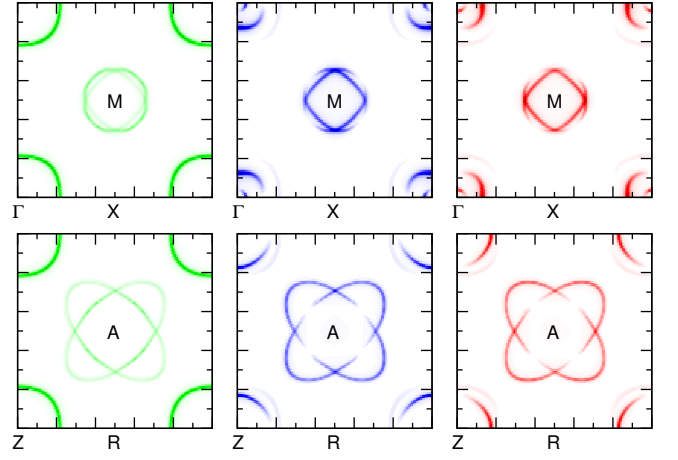

FIG. S2. (Color online) LDA electronic band-structure (top) and LDA+DMFT momentum-resolved spectral function (bottom). [S1] The colors indicate Fe-d and As-p orbital contents: $d_{xz(yz)}$, d_{xy}, are denoted by red and green respectively, while all other orbitals are displayed in blue.

symmetry lines Γ-M and Γ-X, the symmetry reduces to B_1 and A_1, respectively. [S5] All the irreducible representations at the BZ boundary are two-dimensional [S5] which implies that all the Bloch states at any $\mathbf{k}$ on the boundary, including M-X line, are doubly degenerate. This can be seen from Fig. S2. At the M-point, the low-energy doubly degenerate electron-like bands are composed of $(d_{xz}^A + id_{yz}^B, d_{yz}^A - id_{xz}^B)$ with symmetry $A_2 \oplus B_2$ along M-Γ and E along M-X. The doubly degenerate bands with higher binding energy are composed of $(d_{xy}^A + d_{xy}^B, d_{xy}^A - d_{xy}^B)$ with symmetry $B_1 \oplus B_2$ and E along M-Γ and M-X, respectively. [S5]

Fig. S3 and Fig. S4 illustrate respectively the LDA and LDA+DMFT partial spectral weight, $A_{ll}(\mathbf{k}, \omega)$, of Fe t_{2g} orbitals on the Fermi surfaces. The two inner hole pockets are predominantly composed from d_{xz} and d_{yz} orbitals. The smallest hole pocket has strong k_z dispersion and is present only at small k_z, while the middle one has weak k_z dispersion. The large hole-like Fermi surface originates purely from in-plane d_{xy} orbitals and therefore is $2D$ without noticeable k_z dispersion. The electron pockets are made from an admixture of d_{xy}, d_{xz} and d_{yz} orbitals with weak k_z dispersion. The electron pockets intersect at finite k_z and their order flips, i.e., the inner pocket at $k_z = 0$ is the outer pocket at $k_z = \pi/c$. The orbital character of portions of the β_2 pocket oriented towards Γ-points is d_{xy}, while for those portions oriented toward X-point it is d_{xz} or d_{yz}. The β_1 pocket originates made predominantly from d_{xz} and d_{yz} orbitals.

Including interactions with LDA+DMFT, the two inner hole pockets shrink while the outer one expands. The middle hole pocket also deforms and takes on a butterfly shape at small k_z. The electron pockets are moderately expanded and they become closer to each other.
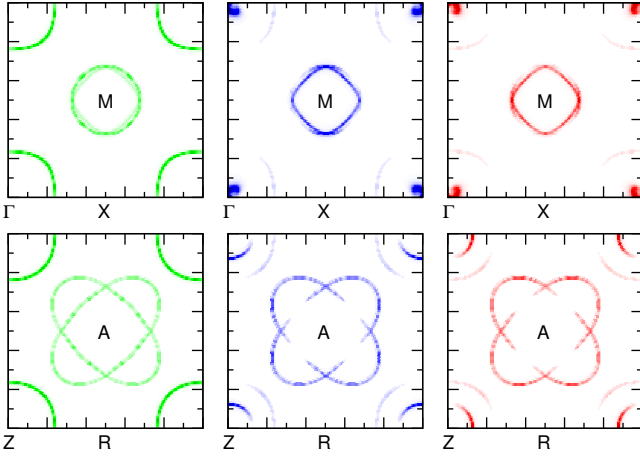
FIG. S4. (Color online) Fe t_{2g} character of the FSs in the k_x-k_y plane with $k_z = 0$ (top panels), and $k_z = \pi/c$ (bottom panels) obtained from the LDA+DMFT calculation. Left, middle and right columns show d_{xy}, d_{xz} and d_{yz} orbitals. The inner hole pocket crosses the Fermi level only in close vicinity to the Γ point and is hard to resolve.

SUPERCONDUCTING INSTABILITY

A superconducting instability in the singlet channel occurs when the pairing susceptibility in this channel diverges as one lowers temperature. A divergent susceptibility signals the appearance of a pole in the corresponding reducible complex vertex function, which describes all scattering processes of two propagating particles. Using the Bethe-Salpeter equation, the reducible vertex function may be written as a function of the irreducible one and of the susceptibility that does not include vertex corrections. We will call this susceptibility bare, even though the Green functions can be dressed. One can then check that the condition for an instability is that an eignvalue of the matrix $-\boldsymbol{\Gamma}^{irr,s}\boldsymbol{\chi}^0_{pp}$ becomes unity. Here $\boldsymbol{\Gamma}^{irr,s}$ is the irreducible vertex function in the singlet channel, and $\boldsymbol{\chi}^0_{pp}$ is the bare susceptibility in the particle-particle channel. [S6, S7] This yields a non-Hermitian eigenvalue problem, equivalent the linearized Eliashberg equation, defined as

$$-(\frac{k_B T}{N})^2 \sum_{K'K'',l_3...l_6} \left[\boldsymbol{\Gamma}^{irr,s}(Q=0)\right]_{K,l_1l_2;K',l_3l_4} \times$$
$$\left[\boldsymbol{\chi}^0_{pp}(Q=0)\right]_{K',l_3l_4;K'',l_5l_6} \boldsymbol{\Delta}_{K'',l_5l_6} = \lambda(T)\boldsymbol{\Delta}_{K,l_1l_2},$$
$$(S1)$$

where $\boldsymbol{\Delta}_{l_1,l_2}(\mathbf{k}, i\omega_m)$ is the gap function which evolves smoothly into the off-diagonal (anomalous) self-energy *below* T_c. [S7] $l_1, \ldots, l_6$ are combined ion (or sublattice) and orbital indices and we have defined $K \equiv (\mathbf{k}, \omega_m)$ as momentum-frequency four-vectors. Even though the eigen-

value problem is non-Hermitian, the leading eigenvalues are real. [S7] The superconducting transition temperature, T_c, can be obtained as the temperature when the maximum (dimensionless) eigenvalue of Eq. (S1) becomes unity. The eigenvalue problem in Eq. (S1) involves diagonalization of a matrix of size $N \times (2N_\omega^{max} + 2) \times N_{orb}^2$ where N in the number of $\mathbf{k}$ points, N_ω^{max} in the maximum number of positive Matsubara frequencies and N_{orb} denotes orbital numbers.

The generalized bare susceptibility in the particle-particle channel is

$$\left[\boldsymbol{\chi}^0_{pp}(0)\right]_{K,l_1l_2;K',l_3l_4} = \frac{N}{2k_B T}\mathbf{G}_{K,l_1l_3}\mathbf{G}_{-K,l_2l_4}\delta_{K,K'},$$
$$(S2)$$

where $\mathbf{G}$ denotes the fully interacting propagator. A factor of $\frac{1}{2}$ in Eq. (S2) arises due to indistinguishability and should be considered to avoid double-counting. [S6] This quantity is plotted in Fig. (3) in the main text without the prefactor $N/k_B T$.

One way to see that the eigenvector of Eq. (S1) is related to the anomalous self-energy is as follows. Consider the one-band case in the BCS approximation. In this approximation one can neglect the frequency dependence of the gap function and of the pairing interaction, which allows to perform the summation on Matsubara frequencies. Using bare propagators in Eq. (S2), one can see that $[(k_B T)^2/N] \sum_{\omega_m} \left[\boldsymbol{\chi}^0_{pp}(0)\right]_{\mathbf{k},i\omega_m;-\mathbf{k},-i\omega_m} = (2n_F(\epsilon_\mathbf{k}) - 1)/4\epsilon_\mathbf{k} = \tanh(\epsilon_\mathbf{k}/2k_B T)/4\epsilon_\mathbf{k}$. Here, n_F denotes the Fermi distribution function and we have used the relation $n_F(\epsilon_\mathbf{k}) = (1 - \tanh(\epsilon_\mathbf{k}/2k_B T))/2$. Inserting this into Eq. (S1), one finds

$$-(\frac{1}{2N}) \sum_\mathbf{k} \left[\boldsymbol{\Gamma}^{irr,s}\right]_{\mathbf{k};\mathbf{k}'} \frac{\tanh(\epsilon_{\mathbf{k}'}/2k_B T)}{2\epsilon_{\mathbf{k}'}}\boldsymbol{\Delta}_{\mathbf{k}'}$$
$$= \lambda(T)\boldsymbol{\Delta}_\mathbf{k}, \qquad (S3)$$

which, for $\lambda = 1$, is the *linearlized* BCS gap equation. The BCS gap equation has the same form as Eq. (S3) but with $\epsilon_\mathbf{k}$ replaced by the quasi-particle excitation $E_\mathbf{k} = \sqrt{\epsilon_\mathbf{k}^2 + |\boldsymbol{\Delta}_\mathbf{k}|^2}$. Considering the Bogoliubov Hamiltonian, one can see that $\boldsymbol{\Delta}_\mathbf{k}$ is the anomalous self-energy.

PAIRING INTERACTION

Evaluation of the effective pairing interaction $\boldsymbol{\Gamma}^{irr,s}$ is a quantum many-body problem. [S6, S7] One way is to employ Parquet equations to formally rewrite it in terms of the fully irreducible vertex function in the singlet channel, $\boldsymbol{\Lambda}^{irr,s}$, and of the vertex ladders in the particle-hole density and magnetic channels, $\boldsymbol{\Phi}_{ph}^{d/m}$, as [S8, S46]

$$[\mathbf{\Gamma}^{irr,s}(Q)]_{Kl_1l_2;K'l_3l_4} = [\mathbf{\Lambda}^{irr,s}(Q)]_{Kl_1l_2;K'l_3l_4} - \frac{1}{2}[\mathbf{\Phi}_{ph}^d(K'-K)]_{-K'l_2l_4;K+Ql_3l_1} + \frac{3}{2}[\mathbf{\Phi}_{ph}^m(K'-K)]_{-K'l_2l_4;K+Ql_3l_1}$$

$$- \frac{1}{2}[\mathbf{\Phi}_{ph}^d(K'+K+Q)]_{-K'l_1l_4;-Kl_3l_2} + \frac{3}{2}[\mathbf{\Phi}_{ph}^m(K'+K+Q)]_{-K'l_1l_4;-Kl_3l_2}, \tag{S4}$$

where a negative sign difference between terms including $\mathbf{\Phi}_{ph}^{d/m}$ and the corresponding terms in Ref. [S6] is compensated by a negative sign difference in definition of susceptibilities (see Eq. (S5) below).

The momentum-frequency appearing as an argument shows the transferred momentum-frequency, while the two momentum-frequency appearing as indices indicate the momentum-frequency of one of the incoming external legs and one of the outgoing ones. In other words, $[\mathbf{\Gamma}^{irr,s}(Q)]_{Kl_1l_2;K'l_3l_4}$ describes the particle-particle scattering of electrons in orbitals l_1, l_2 with momenta/frequencies $(K+Q,-K)$ to electrons in orbitals l_3, l_4 with momenta/frequencies $(K'+Q,-K')$. Here, we are interested in the pairing of electrons at zero center of mass momentum and zero Matsubara frequency, i.e., $Q=0$ component.

The vertex $[\mathbf{\Lambda}^{irr,s}(Q)]_{Kl_1l_2;K'l_3l_4}$ is irreducible in all two-particle channels. It is not singular. Its leading order is given by a linear combination of the irreducible density and magnetic vertices. The vertex ladder functions that appear in Eq. (S4) are important for pairing and are defined as

$$\mathbf{\Phi}_{ph}^{d/m}(Q) = \mathbf{\Gamma}^{irr,d/m}(Q)\boldsymbol{\chi}_{ph}^{d/m}(Q)\mathbf{\Gamma}^{irr,d/m}(Q), \tag{S5}$$

where the right-hand side is a matrix multiplication in K and orbital indices combined. Each matrix multiplication has an implied normalization factor (k_BT/N). The functions $\mathbf{\Gamma}^{irr,d(m)}$ and $\boldsymbol{\chi}_{ph}^{d/m}$ are, respectively, irreducible vertex functions and generalized dressed susceptibilities in the density/magnetic channels. Using the Bethe-Salpeter equation in the particle-hole density/magnetic channels, $\boldsymbol{\chi}^{d/m}$ can be decomposed into bare susceptibility and vertex correction with the help of the irreducible vertex functions:

$$\boldsymbol{\chi}_{ph}^{d(m)}(Q) = \boldsymbol{\chi}_{ph}^0(Q)$$
$$- (+)\boldsymbol{\chi}_{ph}^{d(m)}(Q)\mathbf{\Gamma}^{irr,d(m)}(Q)\boldsymbol{\chi}_{ph}^0(Q). \tag{S6}$$

Again the second term on the right-hand side is a matrix multiplication with the corresponding normalization factor and the bare generalized susceptibility is given by

$$[\boldsymbol{\chi}_{ph}^0(Q)]_{Kl_1l_2;K'l_3l_4} = -(\frac{N}{k_BT})\mathbf{G}_{K+Q,l_1l_3}\mathbf{G}_{K,l_4l_2}\delta_{K,K'}. \tag{S7}$$

For further progress, one has to do some approximation. One can calculate the ladder functions in the particle-hole channel, $\mathbf{\Phi}_{ph}^{d/m}$, by simply replacing all irreducible vertex functions with a static and momentum-independent interaction. This corresponds to the random-phase approximation (RPA). In RPA another simplification appears due to time- and spatial-locality of the vertex functions. This allows to perform the summations over momentum-frequency of the external legs. This greatly simplifies the equations and it also reduces the size of matrices, which now are only functions of transferred momentum-frequency vector and of orbital indices. For example, for the bare susceptibility in the particle-hole channel we obtain

$$[\boldsymbol{\chi}_{ph}^0(Q)]_{l_1l_2;l_3l_4} = -(\frac{k_BT}{N})^2 \sum_{KK'}[\boldsymbol{\chi}_{ph}^0(Q)]_{Kl_1l_2;K'l_3l_4}$$
$$= -(\frac{k_BT}{N}) \sum_{K}\mathbf{G}_{K+Q,l_1l_3}\mathbf{G}_{K,l_4l_2}. \tag{S8}$$

Thus, one can drop the external momentum-frequency in the Parquet equations and rewrite the pairing interaction at $Q=0$ as

$$[\mathbf{\Gamma}^{irr,s}(0)]_{Kl_1l_2;K'l_3l_4} = [\mathbf{\Lambda}^{irr,s}(0)]_{Kl_1l_2;K'l_3l_4}$$
$$- \frac{1}{2}[\mathbf{\Phi}_{ph}^d(K'-K)]_{l_2l_4;l_3l_1} + \frac{3}{2}[\mathbf{\Phi}_{ph}^m(K'-K)]_{l_2l_4;l_3l_1}$$
$$- \frac{1}{2}[\mathbf{\Phi}_{ph}^d(K'+K)]_{l_1l_4;l_3l_2} + \frac{3}{2}[\mathbf{\Phi}_{ph}^m(K'+K)]_{l_1l_4;l_3l_2}. \tag{S9}$$

In the DMFT framework, the irreducible vertices are still local but they become frequency dependent [S9, S10] and in the context of iron pnictide superconductivity have only been calculated in the LDA+DMFT study of Refs. [S11, S12]. However, obtaining the full frequency dependence of the DMFT vertex is numerically very expensive and challenging for the multiorbital systems at the low temperatures. A calculation of the dressed susceptibility in DMFT is possible by quantum Monte Carlo (QMC) in the Hirsch-Fye algorithm [S13] or hybridization expansion algorithm [S14]. The irreducible vertex can be obtained from the dressed susceptibility using Bethe-Salpeter equation. However, both methods have serious limitations. The Hirsch-Fye algorithm is only applicable at very high temperature, which is not suitable for studying superconductivity. In the temperature range accessible by this method, the pairing instability is very weak. The hybridization expansion algorithm gives good results for the dressed susceptibility only at low frequencies. Indeed, the noise grows very fast for moderate and high frequencies. [S15] To extract the irreducible vertex from the dressed susceptibility, using the Bethe-Salpeter equation, requires all frequencies, consequently, even the low frequency data of the full vertex are not usable. Furthermore, even if we assume that

we have the frequency dependent irreducible vertex, the size of eigenvalue problem in the Eliashberg equation for multi-band systems is so large that only a limited number of lowest Matsubara frequencies can be considered. On this limited number of frequencies, the irreducible vertex does not reach its asymptotic behavior. Therefore an RPA analysis with static screened irreducible vertices (representing an average over frequency) seems a better approximation. Hence we take local frequency-independent irreducible vertices. [S16] Since the pnictides are weakly to moderately correlated systems, including the DMFT propagators in the resulting RPA-like equations gives a better description of Fermi surface nesting, and accounts for the interaction of propagating particles with their environment. We think the results should be more reliable than standard LDA+RPA.

Even with the above approximations for $\mathbf{\Phi}_{ph}^{d/m}$ the equation for $\mathbf{\Gamma}^{irr,s}$ depends on the incoming and outcoming momentum-frequency vectors. Thus, full matrices appear in the Eliashberg equation.

To our knowledge, in all the previous studies another approximation, the so called BCS approximation, has been used to solve the Eliashberg equation. In this approximation, since the pairing interaction falls off rapidly on a frequency scale which is small compared with the bandwidth, one can neglect the frequency dependence of the gap function. Furthermore, in this approximation one takes into account only the contribution from the lowest Matsubara frequency, the effective interaction is symmetrized, and its imaginary part is neglected, [S17] making the Eliashberg equation a real symmetric equation. Then the summation over Matsubara frequencies in the bare p-p susceptibility is performed to further simplify the Eliashberg equation. Moreover, often the resulting equation is projected on the Fermi surfaces and is solved assuming a real gap function with a specific symmetry. [S8, S18] Strong coupling treatments such as those of Refs. [S19] and [S20] do not restrict the pairing function to the vicinity of the Fermi surface but do not take into account the retardation of the pairing interaction.

Here, we solve the full equation in the physical 2-Fe Brillouin zone with 10-d orbitals at $k_B T = 0.01$ eV. We use a $16 \times 16 \times 2$ **k**-mesh and 12 Matsubara frequencies. The convergence of the results have been checked by changing the above values to a $8 \times 8 \times 2$ **k**-mesh and 24 Matsubara frequencies. The three largest eigenvalues of the former set are $\simeq 0.125, 0.099, 0.085$ and they change by less than 10% for the second set. More importantly, the gap symmetries do not change between the two sets. The leading channel is conventional s^{+-}, the next-leading channel is anti-phase s^{+-} while the third one has d_{xy} symmetry.

The irreducible vertex function in density/magnetic channels are defined as: $\mathbf{\Gamma}^{irr,d(m)} = \mathbf{\Gamma}^{irr,\uparrow\downarrow} + (-)\mathbf{\Gamma}^{irr,\uparrow\uparrow}$. In RPA, the irreducible vertex function is replaced by the antisymmetrized static Coulomb vertex, $\mathbf{\Gamma}^{0,\sigma\sigma'}$ which, in terms of the interacting part of Hamiltonian $(1/2) \sum_i \sum_{l_1...l_4} \sum_{\sigma\sigma'} I_{l_1 l_2, l_3 l_4}^{\sigma\sigma'} c_{il_1\sigma}^\dagger c_{il_2\sigma'}^\dagger c_{il_3\sigma'} c_{il_4\sigma}$ is de-

fined by $\mathbf{\Gamma}_{l_1 l_2; l_3 l_4}^{0,\sigma\sigma} = I_{l_1 l_4, l_3 l_2}^{\sigma\sigma} - I_{l_1 l_4, l_2 l_3}^{\sigma\sigma}$ and $\mathbf{\Gamma}_{l_1 l_2; l_3 l_4}^{0,\sigma\bar\sigma} = I_{l_1 l_4, l_3 l_2}^{\sigma\bar\sigma}$, where $\bar\sigma \equiv -\sigma$. For a local interaction the following forms for density/magnetic irreducible vertex functions are obtained

$$\mathbf{\Gamma}_{l_1 l_2; l_3 l_4}^{irr,d(m)} = \begin{cases} U_s(U_s) & l_1 = l_2 = l_3 = l_4 \\ -U_s' + 2J_s(U_s') & l_1 = l_3 \neq l_2 = l_4 \\ 2U_s' - J_s(J_s) & l_1 = l_2 \neq l_3 = l_4 \\ J_s'(J_s') & l_1 = l_4 \neq l_2 = l_3 \\ 0 & \text{otherwise} \end{cases}$$
(S10)

where U_s and U_s' denote the screened static local intra- and inter-orbital density-density interactions while J_s and J_s' are Hund's coupling and pair-hopping interactions. Due to locality of the interaction the four orbital indices belong to same ion. We also assume spin rotational invariance so the equalities $U_s' = U_s - \frac{5}{2}J_s$ [S21] and $J_s' = J_s$ are satisfied. Finally, the fully irreducible vertex $[\mathbf{\Lambda}^{irr,s}(Q)]_{Kl_1 l_2; K' l_3 l_4}$ is replaced by $\frac{1}{2}(\mathbf{\Gamma}^{irr,d} + \mathbf{\Gamma}^{irr,m})$ transformed to the particle-particle channel.

In our study we used two sets of screened interaction parameters yielding the same magnetic Stoner factor, namely $J_s = 0.1U_s$, $U_s = 2.4$ eV and $J_s = 0.3U_s$, $U_s = 1.68$ eV. The values for U_s and J_s are relatively standard in the literature that uses the RPA approach for the pairing vertex. They are smaller than cRPA values [S22] in order to account for the RPA overestimation of spin fluctuations. We found that for a given J_s/U_s ratio changing them within a limited range does not change the qualitative aspects of our results for the superconducting state.

RPA SUSCEPTIBILITIES

The top panels of Fig. S5 compare important components of the LDA bare susceptibilities in the particle-hole channel, $\mathbf{\chi}_{ph}^0(\mathbf{q}, \nu_n = 0)$ at $k_B T = 0.01$ eV, with their LDA+DMFT counterpart along a high-symmetry path. The Fe-1 (Fe-2) d_{z^2}, $d_{xy}, d_{x^2-y^2}, d_{xz}, d_{yz}$ orbitals are labeled respectively as 1 (6), 2 (7), 3 (8), 4 (9), and 5 (10). Due to better nesting, [S23] the dominant component of the LDA bare susceptibility is the d_{xy} intra-orbital component, $[\mathbf{\chi}_{ph}^0]_{22;22} (= [\mathbf{\chi}_{ph}^0]_{77;77} = [\mathbf{\chi}_{ph}^0]_{27;27})$, with incommensurate peaks around the M (A) point, which come from nesting between the hole and electron pockets. The inter-orbital d_{xy}-$d_{xz(yz)}$ component, $(24; 24)$ and $(25; 25)$ respectively, is rather large and shows a peak centered at the M (A) point. The intra-orbital $d_{xz(yz)}$ components $(44; 44)$, and the inter-orbital d_{xz}-d_{yz} components $(45; 45)$, have almost the same magnitude in the entire **k**-space. Nesting between the hole (electron) pockets is weak and gives small peaks at small momenta.

Upon introducing correlations within the LDA+DMFT framework, the absolute values of the bare susceptibilities are suppressed for all components. However, the AF fluctuations remain the leading instability. The small peaks due to intra-hole (electron) pockets scattering are shifted towards smaller
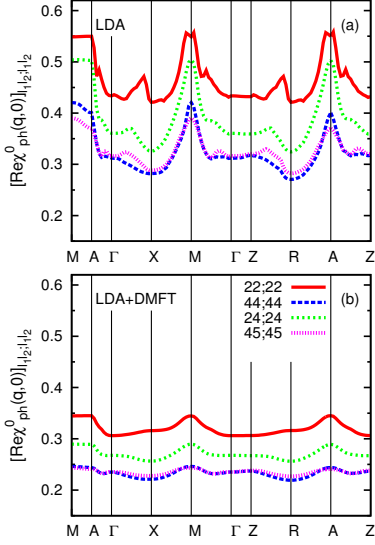
FIG. S5. (Color online) comparison between LDA (panel (a)) and DMFT (panel (b)) components of the bare susceptibility, $[\boldsymbol{\chi}^0_{ph}(\mathbf{q}, \nu_n = 0)]_{l_1 l_2; l_1 l_2}$, of LiFeAs at $k_B T = 0.01$ eV in the particle-hole channel (top panels). For K summation in Eq. (S8) we have used a $32 \times 32 \times 16$ $\mathbf{k}$-mesh and 1024 positive frequencies.
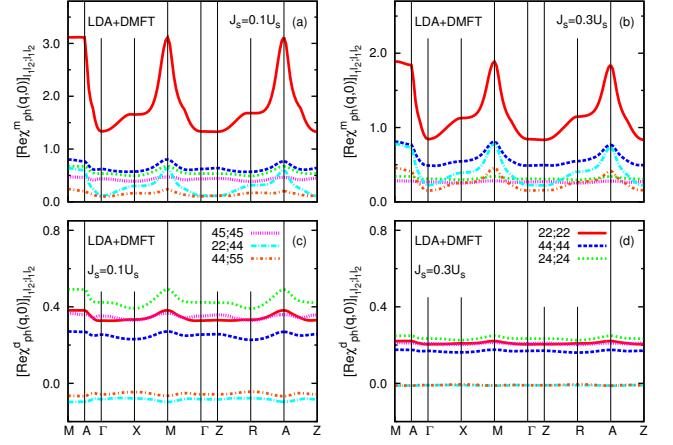

FIG. S6. (Color online) Several components of the dressed susceptibility in, respectively, the magnetic channel, density channel of LiFeAs at $k_B T = 0.01$ eV in the particle-hole channel. There are two sets of screened interaction parameters yielding the same magnetic Stoner factor, namely $J_s = 0.1 U_s$, $U_s = 2.4$ eV on the left and $J_s = 0.3 U_s$, $U_s = 1.68$ eV on the right. Here, J_s denotes Hund's coupling and U_s the local intra-orbital Hubbard interaction. The inter-orbital interaction and pair hopping are determined assuming spin-rotational symmetry. The same line color convention is used in all panels. The convention can be read from the insets of parts (c),(d) of the figure. 2,4,5 stand respectively for d_{xy},d_{xz} and d_{yz}.

momenta and smoothed, resulting in a relative increase of zero momentum scattering.

Fig. S6 show several components of the RPA susceptibility in the density and magnetic channels for two sets of screened interaction parameters that yield the same magnetic Stoner factor. The RPA magnetic (charge)-susceptibility is similar to the bare one but enhanced (reduced) due to the effect of the Coulomb interaction, $\boldsymbol{\chi}^{m(d)}_{ph} = \boldsymbol{\chi}^0_{ph}/[\mathbf{1} - (+)\boldsymbol{\chi}^0_{ph}\boldsymbol{\Gamma}^{m(d)}]$. The form of the irreducible vertex functions, Eq. (S10), shows that a non-zero Hund's coupling breaks spin-orbital symmetry and suppresses orbital fluctuations. This can be seen from a suppression of the charge fluctuation upon increasing J_s (compare panels (c) and (d) of the Fig. S6). The magnetic susceptibility is also clearly larger than the density susceptibility. This translates into a repulsive effective pairing interaction. This is more pronounced for the intra-orbital components in general and in particular for d_{xy}. The inter-orbital components $[\boldsymbol{\chi}^{m(d)}_{ph}]_{l_1 l_2; l_1 l_2}$, with for example l_1, l_2 given by (24) d_{xy}-d_{xz} or (45) d_{xz}-d_{yz} in Fig. S6, are susceptibilities which in RPA are enhanced by inter-orbital Coulomb interaction, as can be seen by comparing with Fig. S5(b).

Interestingly, upon increasing the J_s/U_s ratio from Fig. S6(a) to Fig. S6(b), the d_{xy} intra-orbital component $[\boldsymbol{\chi}^m_{ph}]_{22;22}$ decreases while the d_{xy}-$d_{xz(yz)}$ and d_{xz}-d_{yz} inter-orbital components $[\boldsymbol{\chi}^m_{ph}]_{22;44(55)}$ and $[\boldsymbol{\chi}^m_{ph}]_{44;55}$ increase slightly. Recall that the calculation is done for a given Stoner factor (proximity to magnetic transition). For $J_s/U_s = 0.3$ the value of U_s is smaller than for $J_s/U_s = 0.1$. One would have expected that with a smaller U_s intra-orbital magnetic correlations would have decreased for all orbitals. Instead, only d_{xy} seems strongly affected. This suggests that the larger

value of J_s not only increases inter-orbital spin susceptibility, as expected, it also increases intra-orbital spin susceptibility in the less strongly correlated orbitals. It is as if, through J_s, spin fluctuations in the more correlated d_{xy} orbital increase those in the other two t_{2g} orbitals. This behavior of the magnetic susceptibility reflects itself directly in the pairing interaction. Furthermore, due to the negative sign of the corresponding off-diagonal dressed susceptibility in the charge channel, the magnetic and charge channels for the inter-orbital components cooperate to boost the corresponding pairing vertex.

Bare particle-particle susceptibility The generalized bare susceptibility in the p-p channel also enters the gap equation. Fig. S7 shows the real part in (a, c) and the imaginary part in (b, d) for several components of the generalized p-p bare susceptibility at the lowest fermionic/bosonic frequencies. The intra-orbital components are purely real. Both real and imaginary parts show relatively sharp peaks at the position of FSs. Panels (c) and (d) show the inter-sublattice components. In the BCS approximation, only real parts survive for the components considered here, due to a summation over Matsubara frequencies. In this case, the inter-orbital pairing is suppressed. Including the imaginary part in the full gap equation changes this trend. The imaginary parts of the inter-orbital components change sign between corner and center of the BZ. They have some symmetries that transfer to the gap function: (i) They are odd under exchange of orbital indices (see Eq. (S18)), as can be seen comparing the green and black lines or the grey and purple lines in Fig. S7(b); (ii) There is also a π phase difference between the two Fe ions (not shown).
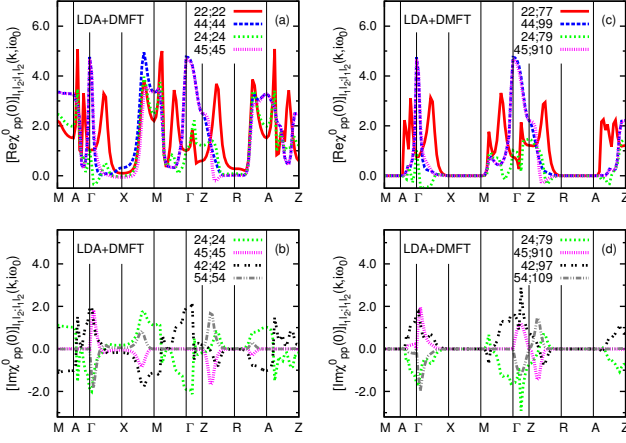
FIG. S7. (Color online) Real part (top) and imaginary part (bottom) of the several intra-sublattice (left) and inter-sublattice (right) components of the generalized particle-particle bare susceptibility at the lowest fermionic/bosonic Matsubara frequency.

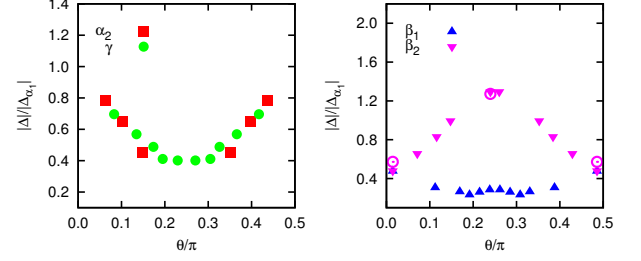FIG. S8. (Color online) For $J_s/U_s = 0.3$, the SC gap magnitude (in units of the average gap magnitude on the α_1 pocket) as a function of the angle θ measured at the Γ and M points with respect to the k_x axis for $k_z = 0$ FSs. Down filled pink triangles are for the β_2 pocket and up filled blue triangles are for the β_1 pocket. The open symbols show the gap magnitude at $\theta/\pi \simeq 0.0, 0.25, 0.5$,, calculated by setting the inter-orbital components to zero. This calculation qualitatively shows that the inter-orbital components reduce the gap magnitude where the electron pockets intersect.

INTER-ORBITAL PAIRING COMPONENTS AND THEIR EFFECTS ON THE SC GAP MAGNITUDE

A quantitative evaluation of the inter-orbital pairing component effects on the SC gap magnitude requires a full disentanglement of the changes caused by the inter-orbital components. This is not a straightforward task, because inter-orbital components are coupled with intra-orbital components in the Eliashberg equations. One way to qualitatively understand their effects is to remove this component from the gap function and recalculate the gap magnitude. As can be seen from Fig. S8, such an analysis shows that the inter-orbital components reduce the gap magnitude, in particular where the electron pockets intersect, which is where these components are maximum. It is worth mentioning that due to anisotropic spin fluctuations in our gauge, [S24] the gap function shows a very small anisotropy. The presented data here are symmetrized.

SYMMETRIES OF GREEN'S FUNCTIONS AND SUSCEPTIBILITIES

The normal Green's function $\mathbf{G}^\sigma_{l_1,l_2}(\mathbf{k},\tau)$ describing the propagation of electrons from l_1 to l_2 with momentum $\mathbf{k}$ is defined as

$$\mathbf{G}^\sigma_{l_1,l_2}(\mathbf{k},\tau) = -\langle T_\tau c_{\mathbf{k}l_1\sigma}(\tau) c^\dagger_{\mathbf{k}l_2\sigma}(0)\rangle,$$

where $c_{\mathbf{k}l_1\sigma}(\tau) = \exp[(H-\mu N)\tau]c_{\mathbf{k}\alpha l_1\sigma}\exp[-(H-\mu N)\tau]$ with τ the imaginary time, $N = \sum_{\mathbf{k}\sigma}\sum_{l_1} c^\dagger_{\mathbf{k}l_1\sigma}c_{\mathbf{k}l_1\sigma}$ the number operator, μ the chemical potential, and T_τ the time-ordering operator. Define $K = H - \mu N$, and Ω as the grand

potential. Then complex conjugation yields

$$\begin{aligned}
\mathbf{G}^\sigma_{l_1 l_2}(\mathbf{k},\tau)^* &= \\
&\Big(-\Theta(\tau)\mathrm{Tr}\big[e^{-\beta(K-\Omega)}e^{K\tau}c_{\mathbf{k}l_1\sigma}e^{-K\tau}c^\dagger_{\mathbf{k}l_2\sigma}\big]^\dagger \\
&+\Theta(-\tau)\mathrm{Tr}\big[e^{-\beta(K-\Omega)}c^\dagger_{\mathbf{k}l_2\sigma}e^{K\tau}c_{\mathbf{k}l_1\sigma}e^{-K\tau}\big]^\dagger\Big) \\
&= -\langle T_\tau c_{\mathbf{k}l_2\sigma}(\tau)c^\dagger_{\mathbf{k}l_1\sigma}(0)\rangle = \mathbf{G}^\sigma_{l_2 l_1}(\mathbf{k},\tau). \quad (S11)
\end{aligned}$$

Transforming to Mastubara frequency space we obtain

$$\mathbf{G}^\sigma_{l_1 l_2}(\mathbf{k},i\omega_m)^* = \mathbf{G}^\sigma_{l_2 l_1}(\mathbf{k},-i\omega_m). \quad (S12)$$

This property of the Green's function implies for the bare susceptibility in the p-h channel,

$$[\boldsymbol{\chi}^0_{ph}(\mathbf{q},i\nu_n)]^*_{l_1 l_2; l_3 l_4} = [\boldsymbol{\chi}^0_{ph}(\mathbf{q},-i\nu_n)]_{l_3 l_4; l_1 l_2}. \quad (S13)$$

It also gives a similar relation for the generalized bare susceptibility in the p-p channel with zero transferred momentum/frequency, $[\boldsymbol{\chi}^0_{pp}(0)]_{K,l_1 l_2; K',l_3 l_4} \equiv [\boldsymbol{\chi}^0_{pp}(0)]_{l_1 l_2; l_3 l_4}(\mathbf{k},i\omega_m)$, as

$$[\boldsymbol{\chi}^0_{pp}(0)]_{l_1 l_2; l_3 l_4}(\mathbf{k},i\omega_m)^* = [\boldsymbol{\chi}^0_{pp}(0)]_{l_3 l_4; l_1 l_2}(\mathbf{k},-i\omega_m). \quad (S14)$$

If the time-reversal symmetry is respected then the Green's function transforms as

$$\begin{aligned}
\mathcal{T}\mathbf{G}^\sigma_{l_1 l_2}(\mathbf{k},\tau) &= \\
&-\Theta(\tau)e^{\beta\Omega}\mathrm{Tr}\big[c_{-\mathbf{k}l_2\bar\sigma}e^{-K\tau}c^\dagger_{-\mathbf{k}l_1\bar\sigma}e^{K\tau}e^{-\beta K}\big] \\
&+\Theta(-\tau)e^{\beta\Omega}\mathrm{Tr}\big[e^{-K\tau}c^\dagger_{-\mathbf{k}l_1\bar\sigma}e^{K\tau}c_{-\mathbf{k}l_2\bar\sigma}e^{-\beta K}\big] \\
&= -\langle T_\tau c_{-\mathbf{k}l_2\bar\sigma}(\tau)c^\dagger_{-\mathbf{k}l_1\bar\sigma}(0)\rangle = \mathbf{G}^{\bar\sigma}_{l_2 l_1}(-\mathbf{k},\tau)
\end{aligned}$$
$$(S15)$$

where we have used $\mathcal{T}|\uparrow\rangle = -ie^{-i\delta}|\downarrow\rangle$ and $\mathcal{T}|\downarrow\rangle = ie^{-i\delta}|\uparrow\rangle$ with $e^{-i\delta} = i$. Note that d-orbitals in cubic symmetry are time-reversal invariant. It can be seen from their definition in terms of Y_l^m.

Transforming to Mastubara frequency, the above equality is expressed in frequency space as

$$\mathbf{G}^{\sigma}_{l_1,l_2}(\mathbf{k}, i\omega_m) = \mathbf{G}^{\bar{\sigma}}_{l_2,l_1}(-\mathbf{k}, i\omega_m). \tag{S16}$$

Combining with the earlier results obtained for complex conjugation, we obtain the following identity

$$\mathbf{G}^{\sigma}_{l_1,l_2}(\mathbf{k}, i\omega_m) = \mathbf{G}^{\bar{\sigma}}_{l_1,l_2}(-\mathbf{k}, -i\omega_m)^*, \tag{S17}$$

which for the generalized bare susceptibility in the p-p channel, Eq. (S2), gives (assuming SU(2) symmetry)

$$\left[\boldsymbol{\chi}^0_{pp}(0)\right]_{K,l_1 l_2;K',l_1 l_2} = \frac{N}{2k_B T} \mathbf{G}_{K,l_1 l_1} \mathbf{G}_{-K,l_2 l_2} \delta_{K,K'}$$

$$= \frac{N}{2k_B T} \mathbf{G}^*_{-K,l_1 l_1} \mathbf{G}^*_{K,l_2 l_2} \delta_{K,K'} = \left[\boldsymbol{\chi}^0_{pp}(0)\right]^*_{K,l_2 l_1;K',l_2 l_1}. \tag{S18}$$

[S1] K. Haule, C.-H. Yee, and K. Kim, Phys. Rev. B **81**, 195107 (2010).

[S2] J. Ferber, K. Foyevtsova, R. Valentí, and H. O. Jeschke, Phys. Rev. B **85**, 094505 (2012).

[S3] S. V. Borisenko, V. B. Zabolotnyy, D. V. Evtushinsky, T. K. Kim, I. V. Morozov, A. N. Yaresko, A. A. Kordyuk, G. Behr, A. Vasiliev, R. Follath, and B. Büchner, Phys. Rev. Lett. **105**, 067002 (2010).

[S4] P. M. R. Brydon, M. Daghofer, C. Timm, and J. van den Brink, Phys. Rev. B **83**, 060501 (2011).

[S5] V. Cvetkovic and O. Vafek, Phys. Rev. B **88**, 134510 (2013).

[S6] N. E. Bickers, "Self-consistent many-body theory for condensed matter systems," (Springer-Verlag, New York, 2004) Chap. 6, pp. 237–296.

[S7] G. Esirgen and N. E. Bickers, Phys. Rev. B **57**, 5376 (1998).

[S8] S. Graser, T. A. Maier, P. J. Hirschfeld, and D. J. Scalapino, New Journal of Physics **11**, 025016 (2009).

[S9] A. Toschi, A. A. Katanin, and K. Held, Phys. Rev. B **75**, 045118 (2007).

[S10] G. Rohringer, A. Valli, and A. Toschi, Phys. Rev. B **86**, 125114 (2012).

[S11] Z. P. Yin, K. Haule, and G. Kotliar, Nat. Phys. **10**, 845 (2014).

[S12] A. Toschi, R. Arita, P. Hansmann, G. Sangiovanni, and K. Held, Phys. Rev. B **86**, 064411 (2012).

[S13] J. E. Hirsch and R. M. Fye, Phys. Rev. Lett. **56**, 2521 (1986).

[S14] E. Gull, A. J. Millis, A. I. Lichtenstein, A. N. Rubtsov, M. Troyer, and P. Werner, Rev. Mod. Phys. **83**, 349 (2011).

[S15] H. Hafermann, K. R. Patton, and P. Werner, Phys. Rev. B **85**, 205106 (2012).

[S16] T. A. Maier, M. Jarrell, and D. J. Scalapino, Phys. Rev. B **75**, 134519 (2007).

[S17] Y. Wang, A. Kreisel, V. B. Zabolotnyy, S. V. Borisenko, B. Büchner, T. A. Maier, P. J. Hirschfeld, and D. J. Scalapino, Phys. Rev. B **88**, 174516 (2013).

[S18] F. Ahn, I. Eremin, J. Knolle, V. B. Zabolotnyy, S. V. Borisenko, B. Büchner, and A. V. Chubukov, Phys. Rev. B **89**, 144513 (2014).

[S19] R. Yu, P. Goswami, Q. Si, P. Nikolic, and J. X. Zhu, Nat Commun **4**, 2783 (2013).

[S20] J. Hu and H. Ding, Sci. Rep. **2**, 381 (2012).

[S21] P. J. Hirschfeld, M. M. Korshunov, and I. I. Mazin, Reports on Progress in Physics **74**, 124508 (2011).

[S22] T. Miyake, K. Nakamura, R. Arita, and M. Imada, Journal of the Physical Society of Japan **79**, 044705 (2010), http://journals.jps.jp/doi/pdf/10.1143/JPSJ.79.044705.

[S23] T. Hajiri, T. Ito, R. Niwa, M. Matsunami, B. H. Min, Y. S. Kwon, and S. Kimura, Phys. Rev. B **85**, 094509 (2012).

[S24] R. Nourafkan and A.-M. Tremblay, ArXiv e-prints (2016), arXiv:1601.05813.